

Article

Impact of Tuned Oxidation on the Surface Energy of Sintered Samples Produced from Atomised B-Doped Al-Cu-Fe Quasicrystalline Powders

Monika Kušter ^{1,2,*}, Janez Kovač ³, Zoran Samardžija ¹, Matej Komelj ¹, Sorour Semsari Parapari ¹, Matejka Podlogar ¹, Jean-Marie Dubois ^{1,2} and Sašo Šturm ^{1,2,4,*}

¹ Department for Nanostructured Materials, Jožef Stefan Institute, Jamova Cesta 39, 1000 Ljubljana, Slovenia

² Jožef Stefan International Postgraduate School, Jožef Stefan Institute, Jamova Cesta 39, 1000 Ljubljana, Slovenia

³ Department for Surface Engineering, Jožef Stefan Institute, Jamova Cesta 39, 1000 Ljubljana, Slovenia

⁴ Department of Geology, Faculty of Natural Sciences and Engineering, University of Ljubljana, Aškerčeva Cesta 12, 1000 Ljubljana, Slovenia

* Correspondence: monika.kuster@ijs.si (M.K.); saso.sturm@ijs.si (S.Š.)

Abstract: Super-hydrophobic surfaces and coatings have stimulated a great deal of research, with the aim being to achieve better wetting properties. Factors such as surface chemistry and roughness play an important role in changing the surface energy, which in turn leads to changes in the wettability. Here, we have analysed the time dependence of the oxide layer and possible surface adsorbates on the surface topography of an Al₅₉Cu₂₅Fe₁₃B₃ quasicrystalline material in relation to changes in the wettability. The quasicrystalline matrix phase was 94% of the sample volume, and it was covered by a very smooth, amorphous oxide layer. The AlB₁₂ and AlFe₂B₂ boron-rich phases were embedded in the quasicrystalline material as a result of the 3 at.% boron addition, which made atomisation of the material a simpler process. Under ambient conditions, the sample was naturally covered by an oxide layer; therefore, it is referred to as “surfenergy” to distinguish it from the conventional surface energy of a bare quasicrystal surface. The growth of the oxide layer with atmospheric ageing and annealing at 500 °C in air for various times was investigated for both cases. The phase most prone to oxidation was the boron-rich AlFe₂B₂, which influenced the topography of the surface and accordingly the wetting behaviour of the specimen. We demonstrated that the surfenergy depends on the polar component, which is the most sensitive to the operating conditions. A correlation between the surfenergy components and the surface roughness was found. In addition, theoretical models to determine the wettability were included.

Keywords: contact angle; surface energy; XPS; microstructure; SEM; TEM; wettability



Citation: Kušter, M.; Kovač, J.; Samardžija, Z.; Komelj, M.; Semsari Parapari, S.; Podlogar, M.; Dubois, J.-M.; Šturm, S. Impact of Tuned Oxidation on the Surface Energy of Sintered Samples Produced from Atomised B-Doped Al-Cu-Fe Quasicrystalline Powders. *Crystals* **2023**, *13*, 859. <https://doi.org/10.3390/cryst13060859>

Academic Editor: Bolv Xiao

Received: 18 April 2023

Revised: 10 May 2023

Accepted: 18 May 2023

Published: 23 May 2023



Copyright: © 2023 by the authors. Licensee MDPI, Basel, Switzerland. This article is an open access article distributed under the terms and conditions of the Creative Commons Attribution (CC BY) license (<https://creativecommons.org/licenses/by/4.0/>).

1. Introduction

The discovery of quasicrystals in melt-spun Al–Mn ribbons by Shechtman et al. in 1982 [1] triggered a revolution in crystallography and changed our understanding of the structure of solids. Just a few years later, the existence of a thermodynamically stable quasicrystal was reported in the Al–Cu–Fe system by Tsai et al. [2]. A stable quasicrystal can have several interesting properties, such as a high hardness, a low coefficient of friction, a low surface energy and a high oxidation and corrosion resistance [3,4]. These properties are appropriate for technological applications such as low-stick surfaces or mechanical devices with reduced friction [5]. Therefore, it is necessary to assess the surface energy of a quasicrystal material that comes into contact with an antagonist such as water or a lubricant in low-stick applications [6] or a solid such as hard steel in mechanical applications [7]. Among the methods used for surface-energy investigations, the sessile droplet technique is convenient for laboratory experiments. The measurements yield a contact angle Θ between

the droplet of the test liquid and the surface of interest, neglecting the equilibrium pressure (π_e) of the adsorbed vapour from the liquid. The Young equation defines the angle Θ at equilibrium between the solid, the liquid, and its vapour:

$$\cos \Theta \gamma_{lv} = \gamma_{sv} - \gamma_{sl} \quad (1)$$

where γ_{sv} , γ_{lv} and γ_{sl} are the solid–vapour, liquid–vapour, and solid–liquid interfacial tensions [8].

At thermodynamic equilibrium, the solid–vapour interfacial tension γ_{sv} is usually taken as the solid surface energy γ_s . Similarly, the interfacial tension γ_{lv} is the liquid surface energy γ_l . The authentic surface energy is determined as the surface excess free energy per unit area of a particular crystal facet and is a physical property of the material. The state of the solid surface can be quantified through the surface energy [9]. It determines the equilibrium shape of the crystal and the adhesion energy at the interfaces with other materials. It also plays an essential role in roughening, faceting, crystal growth and in the nucleation kinetics of precipitates [10]. The surface energy can be computed [9] for periodic crystals, for example, some elementary metals: $\gamma_{Al} = 1200 \text{ mJ/m}^2$, $\gamma_{Fe} = 2200 \text{ mJ/m}^2$, and $\gamma_{Cu} = 1800 \text{ mJ/m}^2$. Unfortunately, computational methods are restricted to relatively simple compounds and do not apply to complex metallic alloys such as quasicrystals or their approximants with giant unit cells of up to thousands of atoms. Due to the absence of a periodic lattice for the surface energy of a quasicrystal, we have to rely on indirect techniques, for instance, friction experiments in a vacuum [11] or thin-film growth [12]. The typical surface energy γ_{QC} of a quasicrystal is in the range $600\text{--}800 \text{ mJ/m}^2$ for aluminium-based alloys [13], i.e., significantly less than the surface energy of the individual constituents [9]. Theory suggests a reduction in the surface energy of quasicrystals as a consequence of the icosahedral symmetry and the formation of a deep pseudo-gap [13] or the excitation of phason modes [14]. In addition, freshly polished and dried samples have contact angles with water in the range of $100\text{--}120^\circ$, much larger than the contact angle observed for aluminium, the main component of the alloy. This implies a sensitivity to the density of itinerant electrons in the bulk of the quasicrystal, beneath its superficial native oxide. Below $10\text{--}12 \text{ nm}$ of oxide thickness, it has been shown to vary in inverse proportion to the thickness of the oxide [13], suggesting a coupling between the electronic distribution on the liquid molecules (e.g., the electric dipole of the water molecule) on the one hand and the topology of the quasicrystal's Fermi surface on the other [15]. The same trend was observed with water deposited on Al-based quasicrystalline coatings [16–19] and films [20], with quasicrystal-reinforced composites [21], and even with liquid metals on Al–Co approximants [22].

These quasicrystals, however, are always covered by a native oxide layer when exposed to the atmosphere. The amorphous alumina layer formed after a very brief time is a few nanometres thick [23]. Annealing above room temperature, typically at $500 \text{ }^\circ\text{C}$, leads to the significant growth of the oxide layer and causes the partition of the chemical species below the layer due to the migration of Al atoms to feed the growth of the oxide [24]. These studies were performed with laboratory samples made of the pure QC phase. Technological applications require the preparation of the material under industrial conditions, using raw materials with an acceptable economic cost, containing impurities, and following an industrial protocol that does not necessarily provide a perfect quasicrystalline material [23]. For instance, commercially available precursor quasicrystalline powders can be applied to prepare surface coatings via plasma spraying. These coatings need to be additionally heat treated after the deposition to eliminate undesirable crystalline phases that endanger the corrosion resistance of the coating and provoke the formation of the QC phases [25]. The main property affecting this behaviour is the surface energy. However, as the material is covered by an oxide layer, we probe not the surface energy of the metallic material but rather the surface energy of the material containing the oxide layer. To avoid confusion between these two entities, we coin a particular word to label the surface energy probed on top of the oxide layer: “surfenergy”. The surfenergy is a few tens of mJ/m^2 and it should

not be confused with the surface energy of the bare metallic materials found underneath the oxide, which is in the range of several hundred mJ/m^2 or more. In reality, the surfaces have physical (e.g., roughness) and chemical (e.g., functional groups) heterogeneities. The influences of various surface heterogeneities were studied by Wenzel [26] and Good [27] (for physical heterogeneity) and Cassie [28] (for chemical heterogeneity). Oxidation behaviour has an influence on the physical properties of the interface, especially at elevated temperatures, and it is relevant for technological applications and determines the viability of valuable materials [13,23,29].

This article reviews the surface behaviour of a sample made from atomised powder via sintering at a temperature close to the peritectic reaction, leading to quasicrystal growth. We study the equilibrium shape of the droplets of two different liquids, which are placed in contact with the surface of a quasicrystalline material based on Al, Cu, Fe and B. The goal is to investigate the oxidation behaviour of the quasicrystalline sample in the air and to determine to what extent the constituent species take part in the formation of the oxide layer.

2. Experimental Details and Analytical Methods

2.1. Sample Preparation

An atomised powder with the nominal composition $\text{Al}_{59}\text{Cu}_{25}\text{Fe}_{13}\text{B}_3$ (at.%) was purchased from the Saint-Gobain company. It forms a stable icosahedral quasicrystal of the Mackay type and an FCC lattice in six dimensions [23]. The powder was produced in a large-scale atomisation tower for industrial purposes. The addition of 3 at.% boron was intended to decrease the alloy's melting point [30]. This powder was mechanically sieved in the range of 20–70 μm and sintered under an argon flow using a uniaxial sintering furnace operated at 930 °C and a pressure of 100 MPa [31]. After sintering, a dense orthogonal $11 \times 15 \times 2 \text{ mm}^3$ polygrained quasicrystalline body was obtained and cut (hereafter called “the sample”) for further studies. The largest surface of this sample was water polished to its final surface roughness by applying a finishing 4000 grit abrasive paper. No grinding paste was used during the polishing procedure to avoid trapping any residues in the sample's open pores. The ageing experiment was performed under ambient conditions with an atmospheric humidity of around 40%. During the ageing experiments, the sample was kept in a dust-free box. In the subsequent experiments, the sample was annealed at 500 °C in the air using a resistance box furnace for time periods varying between a few minutes and several hours. The duration of the cooling stage was identical for all the annealing times, with around 5 h needed to reach a temperature of 20 °C. Before every subsequent ageing and annealing period, the specimen's surface was re-polished and dried in a flow of hot air.

2.2. Scanning Electron Microscopy (SEM)

A JEOL JSM-7600F (JEOL, Tokyo, Japan) field-emission-gun scanning electron microscope (SEM) equipped with energy-dispersive X-ray spectroscopy (EDXS) was used to characterise the microstructure and elemental composition of the prepared sample. The quantitative EDXS analyses were performed using the Oxford Instruments INCA Microanalysis Suite with an X-Max 20 SDD detector. The sample used for SEM/EDXS microstructural characterisation was prepared using standard metallographic procedures for aluminium alloys. The investigation was performed on a quasicrystalline sample to examine the phases and surface morphology. Images were taken from the central area of the sample in the SEI and BSE modes of operation to reveal phases with different compositions. The sample was characterised after polishing, ageing at different times in air and after annealing at 500 °C for different times in air.

2.3. X-ray Powder Diffraction (PXRD)

The X-ray powder diffraction (PXRD) data were collected with a Malvern Panalytical Empyrean X-ray (Malvern Panalytical, Almelo, the Netherlands) diffractometer using a monochromated X-ray beam produced by a Cu-target tube ($\lambda\text{K}\alpha_1 = 0.15406 \text{ nm}$ and

$\lambda K\alpha_2 = 0.154439$ nm). The measurements were obtained in Bragg–Brentano geometry by applying a divergence slit of 0.04 rad, in the range of $10^\circ < 2\Theta < 90^\circ$, using a step size of 0.0131° and with a counting time of 1 s per step. The PXRD data were analysed using the HighScore Plus XRD Analysis Software database PDF-4+ 2022 and on the basis of the literature relating to quasicrystals [23].

2.4. X-ray Photoelectron Spectroscopy (XPS)

The XPS analysis was carried out on a PHI-TFA XPS spectrometer produced by Physical Electronics Inc (Chanhassen, Minnesota, MN, USA), and equipped with an Al monochromatic source. The vacuum in the XPS spectrometer was 1×10^{-9} mbar and the analysed area was 0.4 mm in diameter, which did not allow us to spatially resolve between the micro-size crystalline phases present on the surface. The XPS analysis depth profile was between 3 and 5 nm. The XPS depth profiles were obtained by sputtering the sample surface with Ar ions having an energy of 4 keV over an area of 3×3 mm². The sputtering rate was calibrated on Ni/Cr layers of known thickness to be 2.0 nm/min.

2.5. Atomic Force Microscopy (AFM)

The morphology of the QC surface was investigated using a VEECO Dimension 3100 atomic force microscope (AFM, Veeco Instruments Inc., Plainview, NY, USA). Three-dimensional (x–y–z) topographic images of the sample surface were obtained, and the surface roughness were extracted with a sub-nanometre resolution on a height scale (z scale) [32]. The images were scanned using the contact mode with a silicon nitride AFM tip at a scan rate of 1 Hz within an image area of 30×30 μm². The measurements were performed at room temperature in air.

2.6. Focused Ion Beam (FIB) System and Transmission Electron Microscopy (TEM)

For the atomic-scale structural analysis of the oxide layer's thickness, a thin, electron-transparent lamella was prepared in the cross-sectional view using focused ion beam–scanning electron microscopy (FIB–SEM, HeliosNanoLab NL650, Thermo Fisher Scientific Inc., Waltham, MA, USA). Prior to the lamella's preparation, a 30 nm thick carbon layer was deposited on the sample to protect the surface layer during the FIB lamella's preparation. The experimental, high-angle annular dark-field–scanning transmission electron microscopy (HAADF–FSTEM) images were recorded to assess the oxide layer and other bulk phases. The probe Cs-aberration-corrected TEM (JEM-ARM 200CF; JEOL, Tokyo, Japan) was operated at 200 keV, with a spatial resolution of 0.08 nm in STEM mode. The elemental distribution was assessed via standard-less energy-dispersive X-ray spectroscopy in STEM mode (STEM–EDX) using a JEOL Centurio 100 mm² EDXS detector and a Gatan GIF Quantum ER spectrometer (Gatan, Pleasanton, CA, USA). The convergence and collection semi-angles for the probe and the HAADF detector were set to 24 mrad and 68–280 mrad, respectively.

2.7. Contact-Angle Measurements

The contact-angle measurements were performed using a Theta Lite-Biolin Scientific instrument (Biolin Scientific, Göteborg, Sweden) to determine the wettability of the flat surface of the sample. The measurements of the contact angle were performed at room temperature in the air with a relative humidity of 40–50% using purified Milli-Q water as a polar liquid and diiodomethane (CH₂I₂) as a non-polar liquid. The maximum volume of the applied droplets was 10 μL. For an individual experiment, 10 contact-angle measurements of each liquid were carried out, yielding the average value and the standard deviation. After every single set of experiments, the sample was re-polished to avoid contamination of the surface by the previous droplets of diiodomethane. The duration of every experiment using both liquids was approximately 20 min.

2.8. Calculation of the Surfenergy

The surfenergy γ_s appearing in Equation (1) as the solid–vapour interfacial tension γ_{sv} can be calculated from the contact-angle Θ measurement as graphically illustrated in Figure 1a. In contrast, the liquid–vapour interfacial tension γ_{lv} and the solid–liquid contribution γ_{sl} need to be determined from Equation (1). Therefore, it is necessary to perform the measurement of the contact angle with two different liquids. In our case, with water and diiodomethane. The quantities γ_{sv} and γ_{lv} can be decomposed into their dispersive (d) and polar (p) components:

$$\gamma_{sv} = \gamma_{sv}^d + \gamma_{sv}^p \quad (2)$$

$$\gamma_{lv} = \gamma_{lv}^d + \gamma_{lv}^p \quad (3)$$

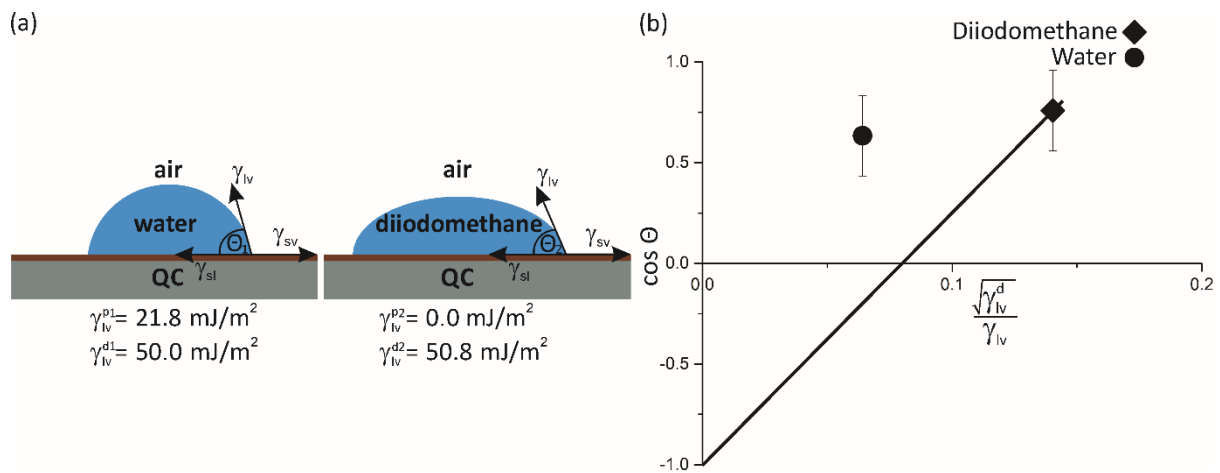


Figure 1. Sketch of a sessile-drop vapour/liquid/solid system. The contact angle is shown (Θ). (a) The shape of a water droplet as a polar liquid on a QC surface, and the shape of a diiodomethane droplet as an apolar liquid on a QC surface with associated components. (b) The plot of the $\cos \Theta$ versus $x = \sqrt{\gamma_{lv}^d / \gamma_{lv}}$ parameter for pure water (labelled by a full circle) and diiodomethane (labelled by a diamond) for our quasicrystalline sample.

The values of the latter for the applied liquids are listed in Table 1.

Table 1. Liquidvapour interfacial tensions, decomposed into the dispersive and polar components for water and diiodomethane, ref. [33].

	Liquid–Vapour Interfacial Tension	Dispersive Component	Polar Component
	γ_{lv} (mJ/m ²)	γ_{lv}^d (mJ/m ²)	γ_{lv}^p (mJ/m ²)
Purified Milli-Q water	72.8	21.8	51.0
Diiodomethane (CH ₂ I ₂)	50.8	50.8	0

To calculate the solid–vapour interfacial tension γ_{sv} (or, equivalently, the surfenergy γ_s), we used the OWRK (Owens, Wendt, Rabel and Kaelble) method [8]. It is based on the assumption that the solid–liquid tension γ_{sl} can be expressed in terms of the geometrical mean of the dispersive and polar components:

$$\gamma_{sl} = \gamma_{sv} + \gamma_{lv} - 2 \left(\sqrt{\gamma_{sv}^d \gamma_{lv}^d} + \sqrt{\gamma_{sv}^p \gamma_{lv}^p} \right) \quad (4)$$

After considering Equations (2) and (3) and inserting Equation (4) into Equation (1) for the two liquids, as denoted by the superscripts 1 and 2, we can derive the following expressions:

$$\gamma_{sv}^d = \frac{1}{4} \left(\frac{\gamma_{lv}^1 \sqrt{\gamma_{lv}^{p2}} (1 + \cos \Theta_1) - \gamma_{lv}^2 \sqrt{\gamma_{lv}^{p1}} (1 + \cos \Theta_2)}{\sqrt{\gamma_{lv}^{d1} \gamma_{lv}^{p2}} - \sqrt{\gamma_{lv}^{d2} \gamma_{lv}^{p1}}} \right)^2 \quad (5)$$

$$\gamma_{sv}^p = \frac{1}{4} \left(\frac{\gamma_{lv}^1 \sqrt{\gamma_{lv}^{d2}} (1 + \cos \Theta_1) - \gamma_{lv}^2 \sqrt{\gamma_{lv}^{d1}} (1 + \cos \Theta_2)}{\sqrt{\gamma_{lv}^{p1} \gamma_{lv}^{d2}} - \sqrt{\gamma_{lv}^{p2} \gamma_{lv}^{d1}}} \right)^2 \quad (6)$$

For the solid–liquid system interacting solely through the dispersion forces and from Equation (4), when an apolar liquid is used, we obtain a linear relation:

$$\cos \Theta = -1 + 2\sqrt{\gamma_{sv}^d} \left(\frac{\sqrt{\gamma_{lv}^d}}{\gamma_{lv}} \right) \quad (7)$$

which yields the dispersive component γ_{sv}^d as the square of the respective line slope.

This approach was formulated by Fowkes [34] in 1950 and confirmed later by other authors, e.g., Fox and Zisman [35] and Dubois [23], on different materials and with different experimental liquids.

3. Results

3.1. Wettability and Surface Energy

Figure 1a presents the shapes of water and diiodomethane droplets on a QC surface with associated components. Figure 1b presents the line defined by Equation (7), which yields the dispersive contribution to the surface energy of the QC covered by a native oxide layer $\gamma_{sv}^d = 39 \text{ mJ/m}^2$.

Figure 2 presents the data from two sets of contact-angle measurements on the QC sample. In the first set of experiments, the ageing time was measured by leaving freshly polished surfaces in air for periods of 5 min, 30 min, 1 h, 2 h, 4 h, 10 h, 18 h, 22 h, 48 h, 96 h and 120 h. In Figure 2a, the representative times are shown. The second set of experiments was determined by varying the annealing time at 500 °C for 10 min, 1 h, 2 h, 4 h and 6 h in air, as shown in Figure 2b with the representative times. The error bars were obtained by repeating the measurements of the contact angles. From the ageing experiment, it is noticeable that at the beginning there is a slight drop in the value of the dispersive component, after which the quantity remains relatively stable and stays in the range of $\gamma_{sv}^d \sim 35\text{--}37 \pm 2 \text{ mJ/m}^2$. In contrast, there is a constant decrease in the polar component with an increasing ageing time from the initial value of $\gamma_{sv}^p = 16 \pm 6 \text{ mJ/m}^2$ down to $2 \pm 4 \text{ mJ/m}^2$. After different annealing times, the dispersive component remains in a similar range as just after ageing. The polar component has a significant drop after annealing for 10 min to 1 h from $\gamma_{sv}^p = 17 \pm 1 \text{ mJ/m}^2$ down to $2 \pm 2 \text{ mJ/m}^2$, whereas this value stabilises between 1 h and 4 h. After annealing for 6 h, the component increases to $\gamma_{sv}^p = 17 \pm 6 \text{ mJ/m}^2$. We can assume that after 6 h of annealing in air, the oxide layer dominates the sample and consequently the overall properties. Furthermore, additional experiments conducted with longer annealing times (e.g., 10 h) show that the surface energy of the solid becomes so large that the droplet of water spreads out and the contact angle becomes too small to be measurable. For a better understanding of the topography of the surface on which the droplet experiments were performed, we implemented roughness analyses after the ageing and annealing experiments. Ageing in air from 5 min to 48 h revealed that the root mean square (R_q) value of the sample was around $6\text{--}8 \pm 0.5 \text{ nm}$, which indicates that the roughness does not significantly develop over time. After annealing at 500 °C for 10 min

and 6 h, the R_q was found to be similar at 18 ± 3 nm, whereas for 1 h it was 12 ± 3 nm and for 4 h, 14 ± 3 nm.

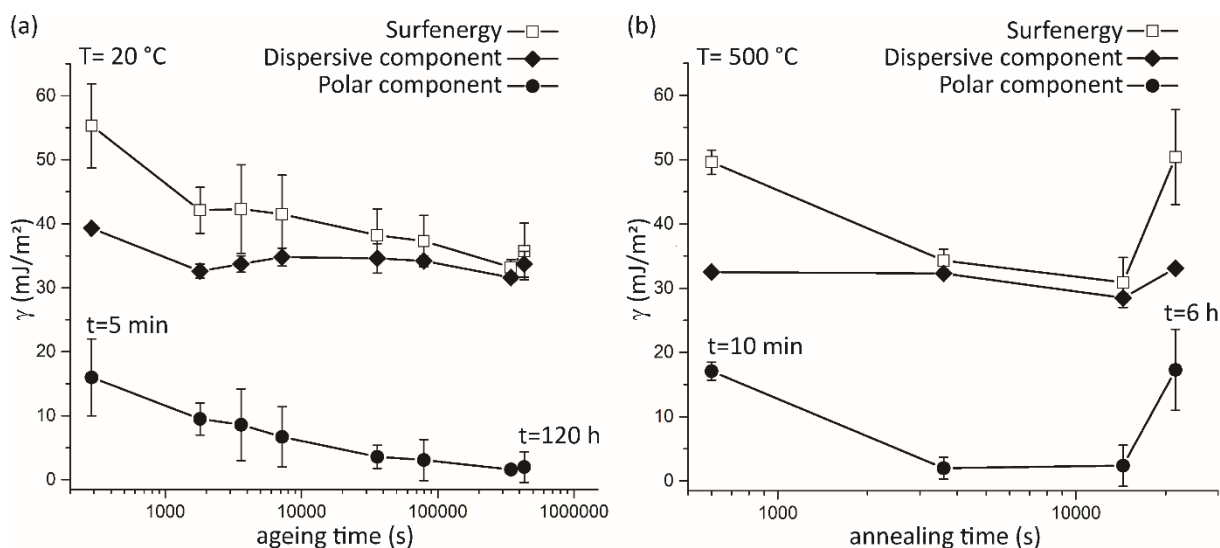


Figure 2. (a) Evolution of the dispersive (solid diamonds) and polar (full circles) components of the total QC surfenergy (open squares) during the ageing experiment at room temperature for different times on a logarithmic scale. Symbols are connected by solid lines to guide the eyes. (b) Variation in the dispersive and polar components of the surfenergy for different annealing times at 500 °C.

For the comparison with the data in Table 2, we measured the two components of the surfenergy on pure copper, pure aluminium and sintered α -Al₂O₃ alumina samples, which are relevant to the present study because all the samples were aged for 5 min. Copper and aluminium are, in ambient air, covered by their native oxides. All three samples were polished as described above and dried in a flow of hot air before the sessile droplet measurements were made. The Al–Cu–Fe–B QC sample contained the Al₆₂Cu₂₅Fe₁₃ matrix and additional boron phases. The data are compared with data taken from the literature for a pure quasicrystalline Al₆₂Cu₂₅Fe₁₃ specimen without boron phases [13].

Table 2. Surfenergy components measured on samples relevant to the present study (pure copper and aluminium metals, sintered α -Al₂O₃ alumina, and the Al–Cu–Fe–B) in comparison to data from the literature.

	Surfenergy	Dispersive Component	Polar Component	
	γ_{sv} (mJ/m ²)	γ_{sv}^d (mJ/m ²)	γ_{sv}^p (mJ/m ²)	
Pure fcc Cu	51 ± 6	39 ± 3	12 ± 3	This work
Pure fcc Al	57 ± 5	39 ± 0.5	18 ± 5	This work
α -Al ₂ O ₃	45 ± 2	39 ± 0.5	6 ± 1	This work
Annealed AlCuFeB	31 ± 4	29 ± 1	2 ± 3	This work
Aged AlCuFeB	45 ± 10	35 ± 5	16 ± 2	This work
Pure icosahedral Al–Fe–Cu	42 ± 10	32 ± 5	20 ± 2	Ref. [23]

3.2. Surface Chemistry

The XPS method was applied to obtain information about the surface chemistry, oxidation states of the elements and their bonds, and about the thickness of the oxide layer on the surface. The high-energy resolution XPS spectra were acquired to gain an insight into the oxidation states of the elements on the surface. Carbon and oxygen were found to be the main elements on the surface. The presence of Al, Fe and Cu cations was also detected, and their concentrations slightly decreased during exposure. The representative XPS spectra C

1s, Al 2p/Cu 3p, Fe 2p and Cu 2p are presented for the ageing time 0.5 h in Figure 3. In the Al 2p spectrum, we identified a peak at 74.3 eV related to Al(3+) and a smaller peak at 72.6 eV related to Al(0). The Cu 3p double peaks at 75.2 eV and 77.6 eV overlapped with the Al 2p peaks. The Fe 2p spectrum exhibits a small component at 706.9 eV related to Fe(0) and peaks at 710.4 eV and 713.0 eV related to the Fe(2+/3+) oxidation states. The Cu 2p_{3/2} spectrum contains a strong peak at 932.5 eV related to Cu(0) and a small peak at 935 eV from the Cu(1+) states. The carbon C 1s spectrum from the surface shows a main peak at 284.8 eV related to the C–C/C–H bonds from the adsorbed carbon species or an adventitious carbon layer. There are also peaks related to the C–O/C–OH bonds at 286.4 eV, C=O bonds at 288.4 eV and a peak at 289.3 eV related to the CO₃ and/or O=C–O bonds. After air exposure for 22 h, some changes were observed in the XPS spectra. These changes were a decrease of the Fe(0) peak and a reduction in the peak at 286.4 for the C–O bonds in the carbon C 1s spectra.

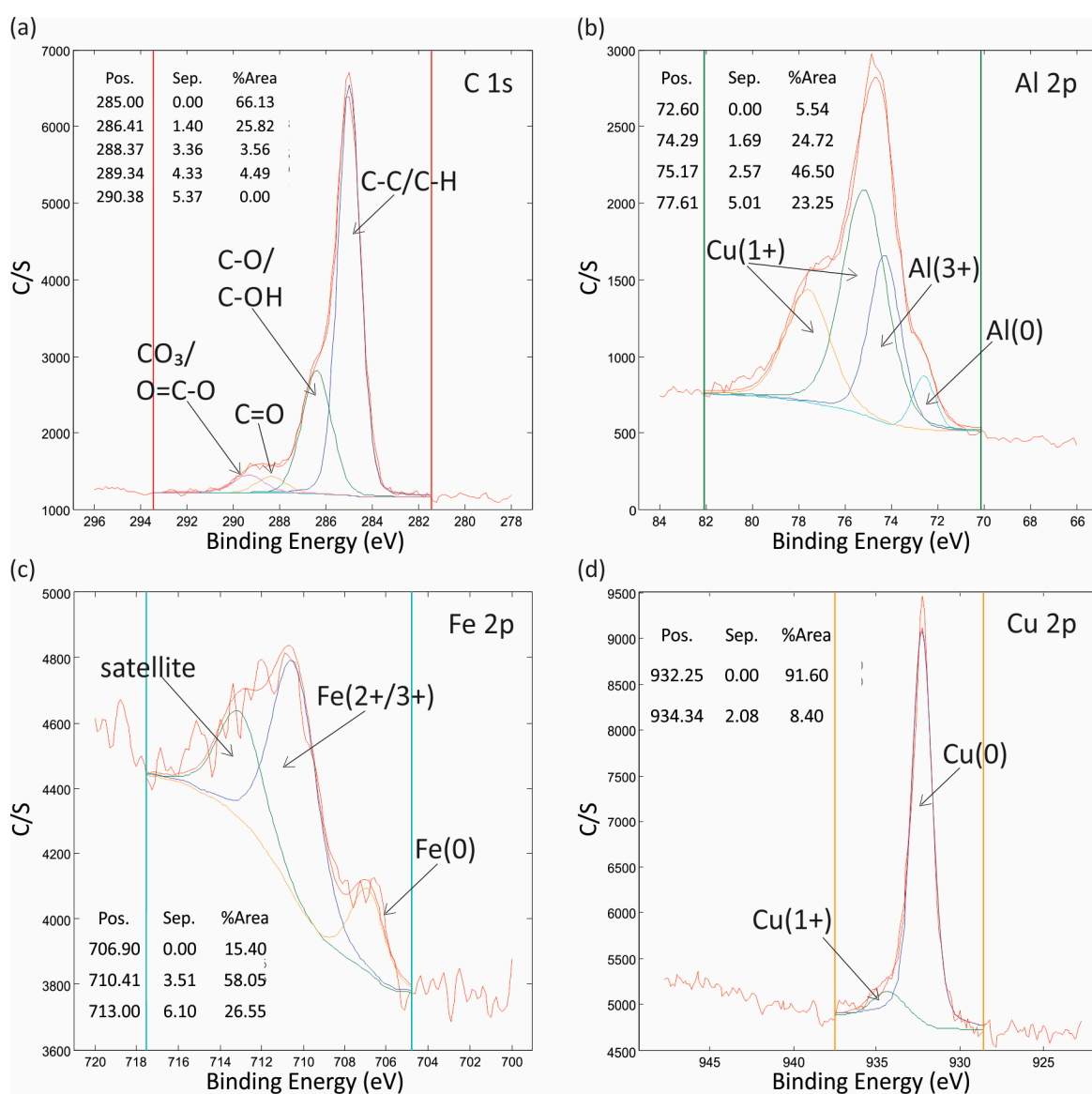


Figure 3. XPS spectra (a) C 1s, (b) Al 2p/Cu 3p, (c) Fe 2p and (d) Cu 2p with the indicated oxidation states measured on the sample surface after ageing for 0.5 h.

In order to obtain information on the chemical composition of the surface oxide layer and the depth distribution in the subsurface region, XPS depth profile measurements were performed on samples after ageing. The XPS depth profiles of the samples exposed for

0.5 h and 22 h in air are presented in Figure 4. From these profiles, it follows that the surface is covered by a thin C-based layer of 0.5–1.0 nm thickness. Beneath the C-based layer, an Al-oxide passivation layer is present. The thickness of the Al-oxide layer was estimated to be 5.0 nm for an exposure of 0.5 h, and it increased by 10% when it was exposed for 22.5 h in air. The B 1s spectrum was detected at a binding energy of 187 eV after removal of the Al-oxide passivation layer. From this, it follows that B is present in the subsurface region at depths of 5 nm and deeper.

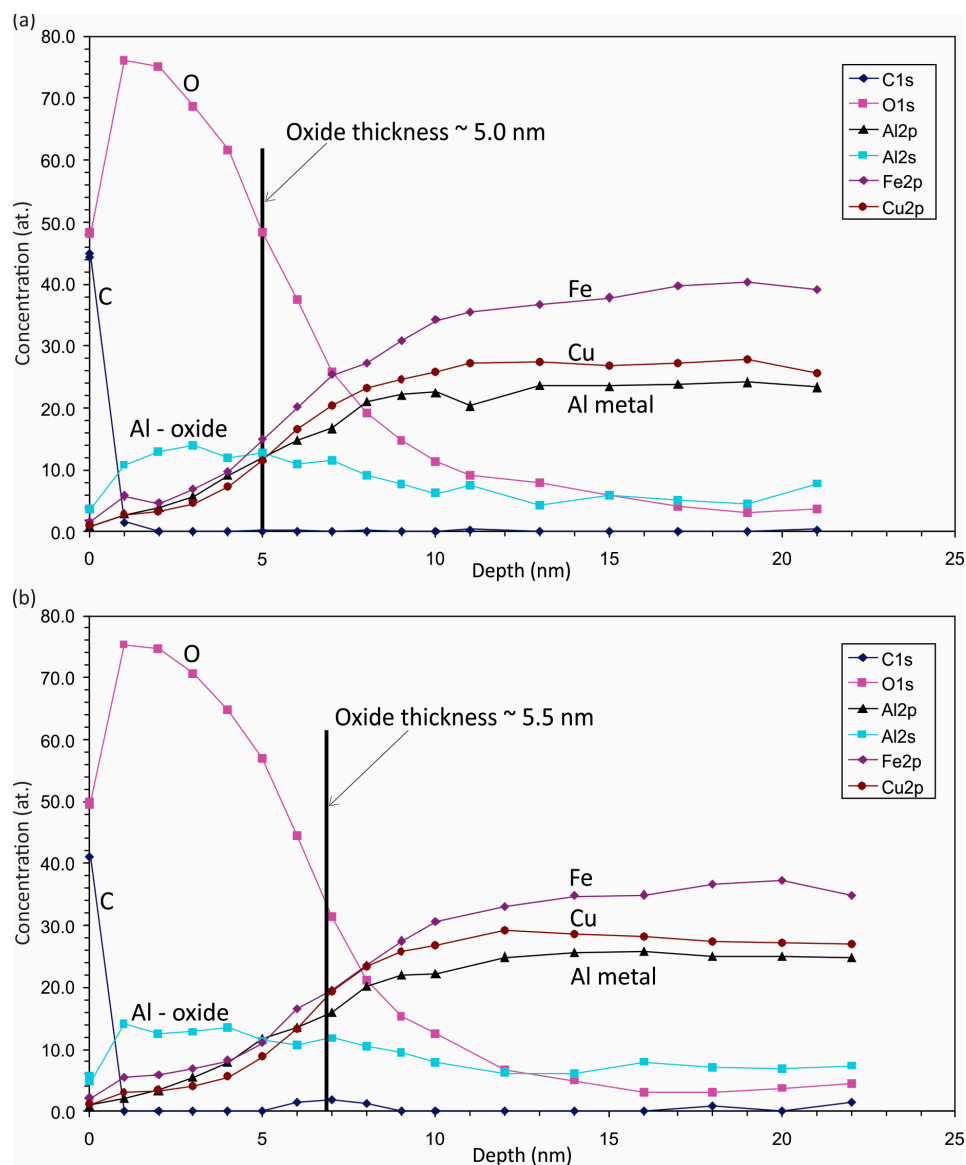


Figure 4. XPS depth profiles of elements measured on the sample after ageing in air at room temperature (a) for 0.5 h and (b) after 22 h.

3.3. The Microstructure and Crystal Phases

The SEM studies investigated the effects of the surface chemistry of different ageing and annealing times in air and explored the morphology of the phases in the QC microstructure. Figure 5a is an SEM image of the overall QC microstructure after different ageing and annealing times. Figure 5b is a representative BSE image of the phases after different ageing and annealing times. Representative microstructures of the phases having different compositions, shapes and sizes are shown in Table 3. For all the experiments, we confirmed the presence of the matrix ternary phase, $\text{Al}_{62}\text{Cu}_{25}\text{Fe}_{13}$, the ternary phase AlFe_2B_2 , the binary β -phase $\text{AlFe}(\text{Cu})$ and precipitates of AlB_{12} . The quasicrystalline *i*-phase matrix

amounted to 94% and was intermixed with 2% of binary β -phase $\text{AlFe}(\text{Cu})$, 2% of ternary AlFe_2B_2 and 2% of AlB_{12} precipitates. However, there might be some uncertainties in the quantitative measured data, as the analytical interaction volume of the method exceeded the physical boundaries of the needle-shaped AlFe_2B_2 phase, probably resulting in a certain convolution between the detected AlFe_2B_2 and the i-phases. We also found a nodular-shaped inclusion of the β -phase, which also contained Cr and Ni. These elements were not part of the powder composition but rather came from residues left in the atomisation tower after the preparation of a previous powder batch (most probably a stainless steel). This is not unusual in the case of an industrial product. The Ni and Cr reacted during the sintering with the Al, Cu and Fe and formed a granule of the β -phase, which cannot be distinguished by means of PXRD from the genuine β -phase of the Al–Fe–Cu system. For a better understanding of the surface, we performed an SEM analysis of the oxidation behaviour after ageing and annealing the material at 500 °C for Figure 5c 1 h and Figure 5d 6 h, respectively. The results suggest that, after ageing and annealing for different times, the morphology did not change significantly for the $\text{Al}_{62}\text{Cu}_{25}\text{Fe}_{13}$ phase, β -phase $\text{AlFe}(\text{Cu})$ and AlB_{12} precipitates. On the other hand, the morphology of the AlFe_2B_2 phase changed drastically after annealing for 1 h and started to grow thicker in layers, and after 6 h, it became very thick with nanocrystalline particles. The amount of oxygen in these samples was at least 25% more than in the aged samples.

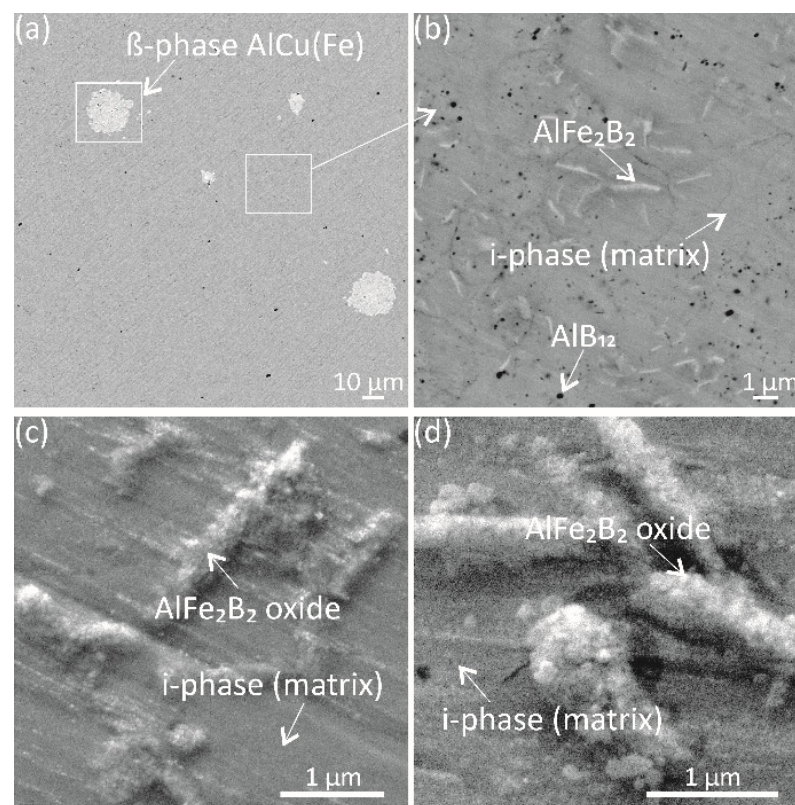
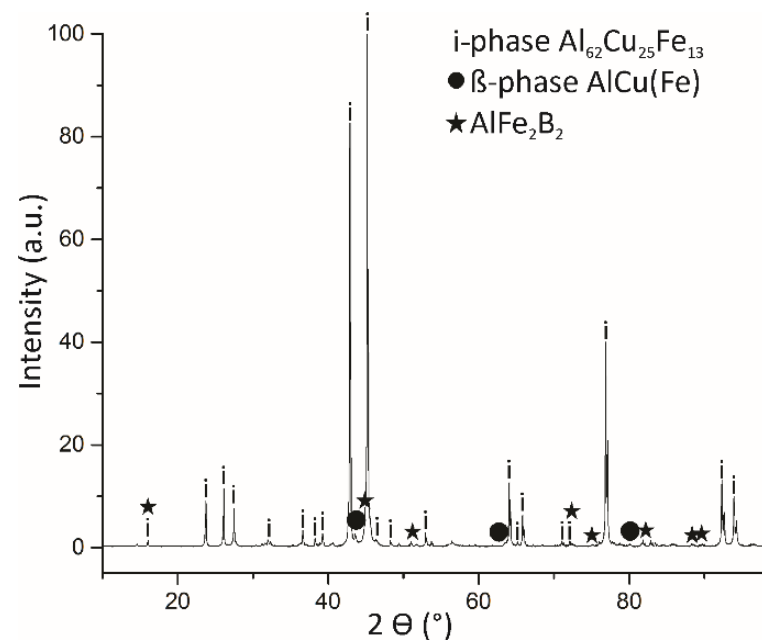


Figure 5. SEM images of the $\text{Al}_{59}\text{Cu}_{25}\text{Fe}_{13}\text{B}_3$ sample when aged and annealed for different times: (a) overall microstructure, (b) characteristic higher-magnification micrograph of the phases, and (c,d) high-magnification micrographs show the growth of the oxide observed on top of the AlFe_2B_2 phase after annealing for 1 h and 6 h at 500 °C, respectively.

Table 3. Chemical composition (in at.%) of the phases inside the quasicrystalline sample with a nominal composition of $\text{Al}_{59}\text{Cu}_{25}\text{Fe}_{13}\text{B}_3$.

Phase Assigned from PXRD	Shape of the Phase	Size of the Phase (μm)	Detected Composition with EDXS (at.%)
i-phase $\text{Al}_{62}\text{Cu}_{25}\text{Fe}_{13}$	Spherical granules	1–5	$\text{Al}_{62}\text{Cu}_{25}\text{Fe}_{13}$
AlFe_2B_2	Needles	2×1	$\text{Al}_{22}\text{Fe}_{24}\text{Cu}_3\text{B}_{51}$
Nodule of β -phase $\text{AlCu}(\text{Fe})$	Flower morphology	10	$\text{Al}_{52}\text{Fe}_8\text{Cu}_{36}\text{Cr}_3\text{Ni}_1$
AlB_{12}	Globules	≥ 1	Al_6B_{94}

The PXRD method provided information about the crystallographic structure of the phases in the microstructure. Figure 6 shows a PXRD pattern obtained from a sintered bulk QC. The diffraction peaks are indexed using the PDF-4+ database and the literature relating to quasicrystals [23]. Three crystal phases could be confirmed. The major phase corresponds to the quasicrystal icosahedral phase (i-phase) and the minor phase is the cubic β - $\text{AlFe}(\text{Cu})$ phase (space group Im-3m , 229). Additional peaks belong to the orthorhombic phase AlFe_2B_2 (space group Cmmm , 65), whereas the peaks corresponding to the AlB_{12} precipitates are too small and they overlap with the i-phase peaks, preventing conformation of the exact crystal structure by means of PXRD. The structure could be either orthorhombic or tetragonal.

**Figure 6.** PXRD pattern of the quasicrystalline material with the nominal composition of $\text{Al}_{59}\text{Cu}_{25}\text{Fe}_{13}\text{B}_3$ (at.%). The highest-intensity peaks belong to the icosahedral phase (i-phase). The other minority phases are β - $\text{AlFe}(\text{Cu})$ and AlFe_2B_2 .

3.4. The Roughness

To gain an insight into the surface morphology of the samples, atomic force microscopy (AFM) measurements were performed. Dramatic changes in the topography of the surface roughness are visible in Figure 7. For calculations of the roughness, we used the root mean square (R_q), an arithmetic mean of the square of the vertical deviation from a reference line. This relates to Equation (8) [36,37], where L is the sampling length of the profile (profile length) and $z(x)$ is a profile in which the profile heights are measured from the reference line.

$$R_q^2 = \frac{1}{L} \int_0^L (z^2) dx \quad (8)$$

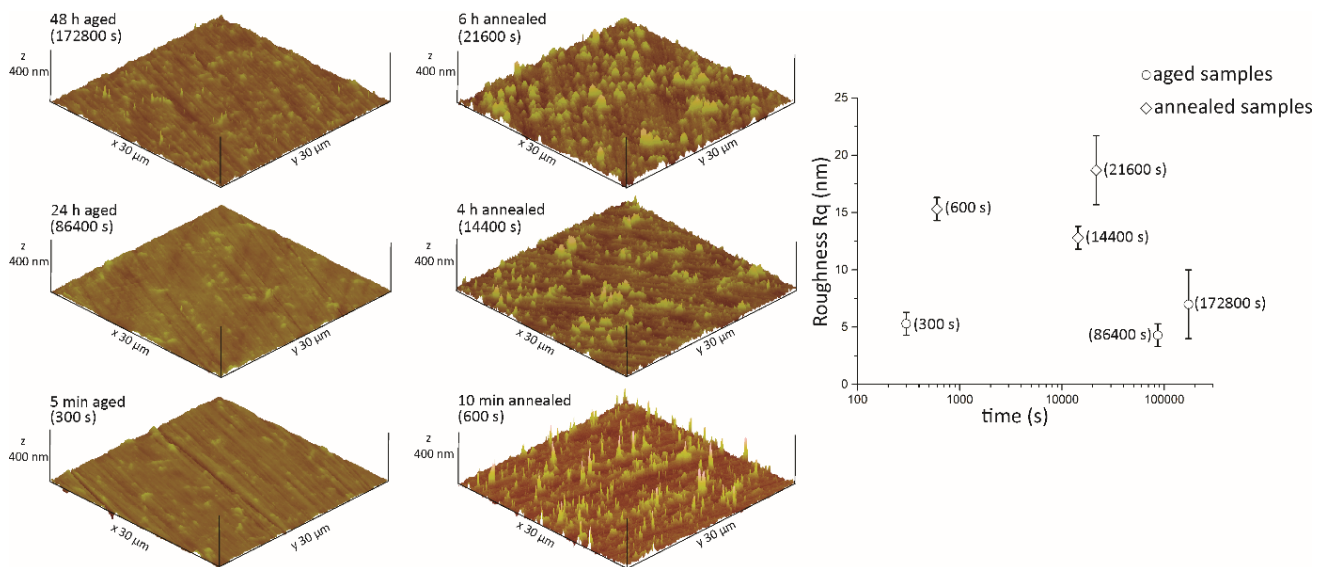


Figure 7. Surface topography and roughness (R_q) of the quasicrystalline material with a nominal composition of $\text{Al}_{59}\text{Cu}_{25}\text{Fe}_{13}\text{B}_3$ (at.%).

It is clear that the growth of the oxide layers during ageing and annealing drastically influences the AlFe_2B_2 phase. On the matrix phase, the oxide particles are more visible after ageing for 48 h and annealing for 4 h and 6 h in air. After 5 min of ageing in air, the oxide layer has broad, dome-like peaks with a height of about 25 nm, whereas after 24 h, small needles become visible; their height is around 20 nm. After 48 h, the needles become larger and sharper, covering the whole area, and grow to around 40 nm high. Very drastic changes in the oxide layer's shape are observed after annealing at 500 °C for various times. After 10 min of annealing, the height of the oxide needles is 160 nm, whereas after 4 h, a dome-like, peak shape is reformed with needles still detectable. At this stage, the vertical height of the layer drops to 100 nm. After 6 h of annealing, the needles disappear, the dome-like peaks are even more pronounced and the vertical height is 160 nm.

3.5. Nanoscale Structure–Chemistry Relationships within the Properties of the Oxide Layer

To understand the transformation of the oxidation phase annealed at 500 °C for 1 h in air, we studied the oxide–metal boundary, while for verification of the existing phases, high-resolution TEM was employed.

Figure 8a is a low-magnification image of the region of surface oxide, and it presents the bulk phases. The chemical composition of the phases was analysed using STEM–EDXS mapping, and the approximate amounts were quantified from a $20 \times 20 \text{ nm}^2$ area. The main region of interest for the quasicrystalline matrix *i*-phase has elements in the amount of Al 60 at.%, Fe 15 at.% and Cu 25 at.%. In the ternary phase AlFe_2B_2 , Al 33 at.% and Fe 67 at.% were detected. It should be noted that elements with a low atomic number, such as boron, cannot be detected with STEM–EDXS measurements. Moreover, for the AlB_{12} , only Al was detected.

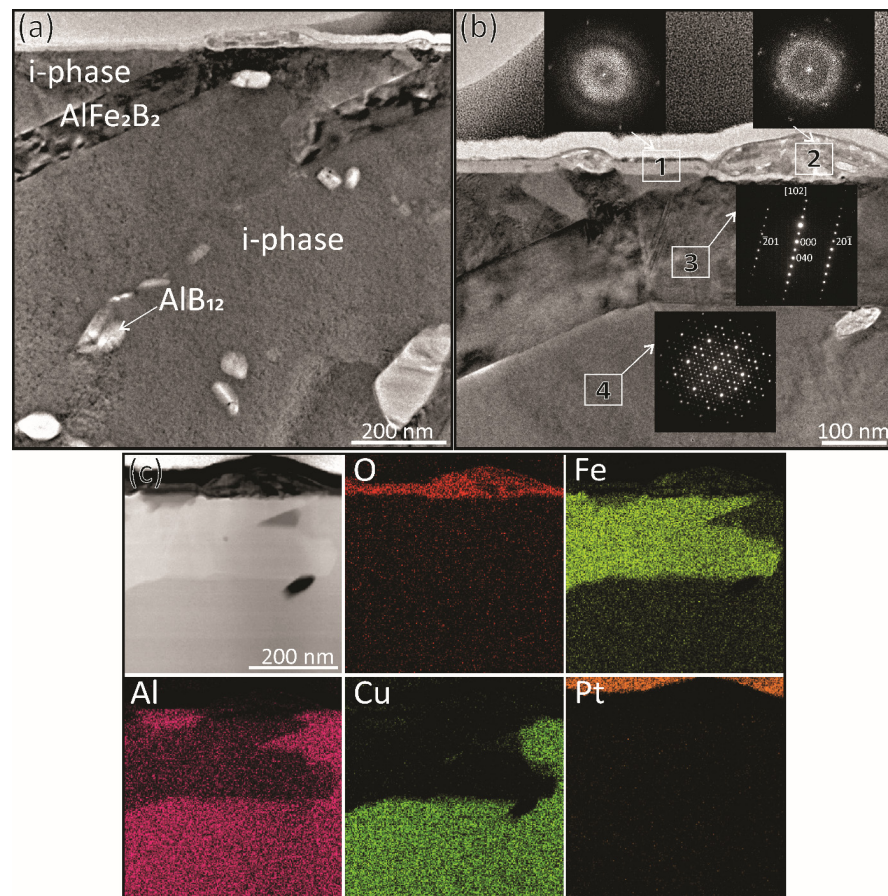


Figure 8. TEM images of the QC annealed at 500 °C for 1 h in air. (a) Overall image with the presented phases in the bulk. (b) High-magnification image of the oxides on the surface labelled as (1) and (2) with the associated FFT pattern of the oxide layer. The insets show the electron-diffraction patterns of the elongated ternary AlFe_2B_2 phase (3) and the i-phase along the 2-fold axis (4). (c) The EDXS mapping of the high-magnification oxide layer above the AlFe_2B_2 phase and the i-phase.

The insets in Figure 8b show the electron-diffraction patterns of the AlFe_2B_2 phase (3) and the i-phase (4). The AlFe_2B_2 phase was indexed as orthorhombic in the zone axis $[102]_{\text{AlFe}_2\text{B}_2}$ and for the i-phase there was a two-fold symmetry. Figure 8b also shows the presence of an oxidised layer on the sample's top surface. For region 1, the EDXS measurements show a composition of Al 33 at.%, Fe 1 at.% and O 66 at.%, which indicates aluminium oxide. Region 2 has a composition of Al 6 at.%, Fe 27 at.% and O 65 at.% for the ternary phase AlFe_2B_2 , which leads to an iron-rich oxide. The thickness of the oxide layer was measured in the quasicrystalline matrix phase to be ~20 nm and in the AlFe_2B_2 phase to be ~50 nm. The FFT of both oxide phases show that it is predominately amorphous, with the presence of some small nanocrystalline areas and presented as the corresponding FFT insets in the figure. Figure 8c shows an EDXS mapping of the high-magnification oxide layer, the AlFe_2B_2 phase and the i-phase. The oxide layer on the i-phase coexists with Al, and on the AlFe_2B_2 phase, the Fe is the major part, with a very small amount of Al.

4. Discussion

The surface oxidation is responsible for the samples' properties, as proven by the XPS analysis, which revealed a diverse chemistry of various carbon-based hydrogen and dangling-oxide bonds on the top-most layer of the aged QC surface. In particular, the revealed oxidation states of the elements deduced from the surface XPS spectra were in accordance with previous studies of the comparable QC systems of Al–Fe–Cu–Cr [29,38], Al–Fe–Cu [39] and Al–Fe–Cu–B [40]. The measured XPS depth profile revealed an enrichment

of the oxide and the aluminium, accompanied by a depletion of the iron and copper in the top surface layer. From this, we concluded that the Al-oxide layer serves as a passivation agent, hindering any further oxidation in the interior of the QC bulk, as previously reported [39]. The electron-diffraction analysis confirmed the presence of the *i*-phase with a two-fold symmetry pattern, which is in agreement with the literature [41], coexisting with an orthorhombic, needle-like AlFe_2B_2 phase and a AlB_{12} phase with a globular morphology. The same was observed by Brien et al. [30] for a sintered Al–Fe–Cu–B alloy. The TEM cross-sectional analysis of the *i*-phase revealed a smooth, 10 nm thick, amorphous, oxide Al-rich layer after the longest ageing time. After annealing at 500 °C for 1 h, the initially amorphous oxide layer on top of the *i*-phase was converted into an aluminium-oxide-rich nanocrystalline film with an average thickness of 20 nm. The needle-like AlFe_2B_2 phase grew in a more complex oxide assembly. The corresponding oxide thickness after annealing for 1 h at 500 °C increased to 50–60 nm, as confirmed by the AFM measurements. The transformation due to annealing was accompanied by a dramatic change in the topography of the surface, which was quantified by a 44% greater roughness in comparison to that of the aged sample. The general composition of the oxide film on the matrix phase is aluminium (33 at.%) and oxygen (66 at.%). The secondary AlFe_2B_2 phase consists of iron (27 at.%), oxygen (65 at.%) and a very small amount of aluminium (6 at.%), while the B content is unknown. As confirmed by the EDXS measurements, the matrix *i*-phase $\text{Al}_{62}\text{Cu}_{25}\text{Fe}_{13}$ and its surface oxide did not exhibit any detectable morphology changes. In contrast, the oxidation of the secondary AlFe_2B_2 phase implies morphological changes after ageing and even more drastically after annealing. This complex oxide grows in different forms, either in terms of sharp needles or dome-like objects, depending on the annealing time.

The amount of boron trapped in the quasicrystalline sample is an additional technological optimisation parameter, where the surface roughness and the resulting surfenergy can be, to some extent, controlled by the amount of B-doping without significantly altering the dominant matrix QC phase. The oxidation behaviour for both cases, during ageing and annealing, exposes different trends for the surface oxidation, which is directly related to the underlying crystal phase. However, the average oxide film thickness remains significantly lower for the aged samples when compared to their annealed counterparts. It can be assumed that the surface energy is also influenced by the subsurface chemistry and not just the formation of the oxide layer and the resulting surface morphology.

The surface roughness and the oxide population influence the surfenergy. The tendency of the QC-treated surfaces to exhibit hydrophobic behaviour can be, in the simplest terms, explained by their increased surface roughness in the nm range. However, it is known that hydrophobic behaviour can be controlled by the surface roughness, as previously shown in reference [26]. As a rule of thumb, the level of hydrophobicity grows with the roughness, which is affected by the shape and size of the oxide forms. On the other hand, there is a relation between the oxides and the two components of the surfenergy.

The changes in roughness are mostly associated with nanocrystalline oxides above the AlFe_2B_2 phase at various time intervals. Namely, for shorter annealing times, the oxide phase is mainly in the form of sharp needles forming above the surface. In contrast, for the longest annealing times, the formation of various oxides becomes largely delocalised in a uniform, dome-shaped oxide layer, populating the sample's surface.

The presence of needles and domes is reflected in an enhanced surface roughness and energy. The latter phenomenon can be explained at the atomistic level by means of the charge accumulation at the tips [42]. A high charge density due to a specific morphology, in our case in the oxides above the secondary phase, is associated with an increased surface energy in comparison with a flat sample, which is in agreement with previous reports (Dubois [23]).

The experimental setup makes it possible to assess the surfenergy using its two main constituents, i.e., the dispersive and polar surfenergy components. To better understand the behaviour of the surfenergy components, a droplet experiment was performed on

different materials (see Table 2). The results revealed a significant difference between our material and the pure aluminium, the main component of the quasicrystalline sample. The dispersive components match to within 8%, because it is less sensitive to the structure, morphology and chemical composition. However, there is a significant difference in the polar components, which is ascribed to the influence of the processing techniques. As highlighted in the following text, in strong contrast to these reference materials, the quasicrystalline sample does exhibit a much lower polar component under suitable preparation conditions. We assigned these differences to coexistence with the majority *i*-phase of a small amount of a needle-like AlFe_2B_2 phase that promotes the formation of specific oxides on the sample surface.

The surface morphology has direct and indirect influences on the behaviour of the liquid droplets. The indirect influence is related to the distribution of electric charges and, consequently, to the energy of the surface, whereas the shape of the droplet is directly affected by the surface landscape.

Conceptually, both polar and dispersive components can contribute to the overall surfenergy. However, as shown in this study, an oxide film thickness of a minimum of 5–10 nm completely masks the QC contribution of the dispersive component, which can be attributed solely to the amorphous oxide layer. Therefore, the dispersive component remains time independent, regardless of the oxide-layer thickness. The only noticeable drop in the dispersive component occurs at an early stage of ageing, when the oxide-layer thickness is sufficiently low (below 5 nm). It is worth mentioning that the droplet experiment for the surfenergy was performed about 5 min after polishing, whereas the XPS measurements were carried out at least 15 min later, preventing us from obtaining an insight into the surface chemistry before complete oxidation. Extremely low values of the dispersive contribution to the QC surface energy, close to the data for polymers (Teflon) in previous studies [13], were obtained by applying a high vacuum and so preventing surface oxidation. Such experiments are of limited technological importance for atmospheric/ambient conditions. Therefore, it is very desirable to prevent excessive oxide-layer growth and to retain the surface influence of the QC electronic states. This can be achieved by means of tuning the sample-processing parameters. The goal is to find a balance between the polar and the dispersive components, since the former is decreased with the ageing/annealing times. The rapid decay of the polar component can be explained by the liquid-molecule reorientation and the surface-charge redistribution due to the electrostatic forces, leading to energy minimisation. This is reflected in the relaxation of the respective atomic positions and the lowering of the surfenergy. The restriction is maintaining the pseudo gap in the electronic structure, which is characteristic of QC materials and apparently responsible for desirable frictional and wetting properties [43].

Since the majority of the oxide layer is formed above the B-containing phase, it might be important to control the content of boron. The amount of boron trapped in the quasicrystalline sample opens an additional technological optimisation parameter, directly influencing the roughness without changing the matrix phase. Utilising the investigated material for future technologies should be focused on the processing optimisation and the boron content related to the interplay between the polar and the dispersive components of the surfenergy.

5. Conclusions

Our research was focused on investigating the wetting behaviour of a quasicrystalline material after ageing at room temperature and annealing at 500 °C for different times in air. The applied sample was made from industrial material and, therefore, contained boron for easier atomisation and lowering the alloy's melting point. The important part of the research looked at the correlation between the surfenergy and the controlled fabrication of the native oxide layer. The study revealed that, after annealing, the AlFe_2B_2 phase was the most prone to oxidation changes and surface morphology. The oxidised layer at the surface

differs from the quasicrystalline matrix phase and the AlFe_2B_2 phase, which exhibits a needles-like morphology and nanocrystallites.

The dispersive component stayed in a similar range after the ageing and annealing experiments since this property is under the influence of the oxidised layer on the material's surface. In both situations, except for the very short ageing time, the dispersive component is found to be experimentally independent. The drastic changes in the polar component were mostly connected to the presence of various hydrogen and dangling-oxide bonds on the very top layer of the QC surface. As a consequence, the surfenergy is dominated by the behaviour of its polar component, which may be tuned over more than an order of magnitude, depending on the oxidation treatment. This information provides a possible route for fine-tuning/engineering quasicrystalline surfaces.

Author Contributions: Conceptualization, M.K. (Monika Kušter), J.-M.D. and S.Š.; Methodology, M.K. (Monika Kušter); Software, M.K. (Matej Komelj); Validation, M.K. (Monika Kušter), J.K., Z.S., M.K. (Matej Komelj), J.-M.D. and S.Š.; Formal analysis, M.K. (Monika Kušter), J.K., Z.S., M.K. (Matej Komelj), S.S.P. and M.P.; Investigation, M.K. (Monika Kušter); Resources, M.K. (Monika Kušter); Data curation, M.K. (Monika Kušter), J.K., Z.S., M.K. (Matej Komelj), S.S.P. and M.P.; Writing—original draft, M.K. (Monika Kušter); Writing—review & editing, J.K., Z.S., M.K. (Matej Komelj), J.-M.D. and S.Š.; Visualization, J.-M.D. and S.Š.; Supervision, J.-M.D. and S.Š.; Project administration, S.Š.; Funding acquisition, S.Š. All authors have read and agreed to the published version of the manuscript.

Funding: This research received no external funding.

Data Availability Statement: Not applicable.

Acknowledgments: This work was performed within the frame of the LIA PACS2 project. The research was financially supported by the Slovenian Research Agency (P2-0084), CNRS and Université de Lorraine, France, and the European Union Horizon 2020 research and innovation programme under grant agreement no. 823717—ESTEEM3.

Conflicts of Interest: The authors declare no conflict of interest.

References

1. Shechtman, D.; Blech, I.; Gratias, D.; Cahn, J.W. Metallic phase with long-range orientational order and no translational symmetry. *Phys. Rev. Lett.* **1984**, *53*, 1951–1953. [[CrossRef](#)]
2. Tsai, A.P.; Akihisa, I.; Tsuyoshi, M. A Stable Quasicrystal in Al-Cu-Fe System. *Jpn. J. Appl. Phys.* **1987**, *26*, L1505. [[CrossRef](#)]
3. Dubois, J.-M. Properties- and applications of quasicrystals and complex metallic alloys. *Chem. Soc. Rev.* **2012**, *41*, 6760–6777. [[CrossRef](#)]
4. Macia, E.; Dubois, J.-M.; Thiel, P.-A. Quasicrystals. In *Ullmann's Encyclopedia of Industrial Chemistry*; Wiley: Hoboken, NJ, USA, 2008. [[CrossRef](#)]
5. Dubois, J.-M.; Weinland, P. Matériaux de Revêtement en Alliage d'Aluminium. Patent No. 2635117, 1988.
6. Dubois, J.-M.; Kang, S.S.; Massiani, Y. Application of quasicrystalline alloys to surface coating of soft metals. *J. Non-Cryst. Solids* **1993**, *153–154*, 443–445. [[CrossRef](#)]
7. Sales, M.; Merstallinger, A.; Brunet, P.; De Weerd, M.C.; Khare, V.; Traxler, G.; Dubois, J.-M. Cold welding and fretting tests on quasicrystals and related compounds. *Philos. Mag.* **2006**, *86*, 965–970. [[CrossRef](#)]
8. Owens, D.K.; Wendt, R.C. Estimation of the surface free energy of polymers. *J. Appl. Polym. Sci.* **1969**, *13*, 1741–1747. [[CrossRef](#)]
9. Vitos, L.; Ruban, A.V.; Skriver, H.L.; Kollár, J. The surface energy of metals. *Surf. Sci.* **1998**, *411*, 186–202. [[CrossRef](#)]
10. Eustatopoulos, B.D.N.; Nicholas, M.G. *Wettability at High Temperatures*; Elsevier: Amsterdam, The Netherlands, 1999; Volume 3.
11. Dubois, J.-M.; De Weerd, M.C.; Brenner, J. A way to estimate the true surface energy of complex metallic alloys. *Ferroelectrics* **2004**, *305*, 159–162. [[CrossRef](#)]
12. Fournée, V.; Ross, A.R.; Lograsso, T.A.; Evans, J.W.; Thiel, P.A. Growth of Ag thin films on complex surfaces of quasicrystals and approximant phases. *Surf. Sci.* **2003**, *537*, 5–26. [[CrossRef](#)]
13. Dubois, J.-M.; Belin-Ferré, E. Wetting and adhesion properties of quasicrystals and complex metallic alloys. *Appl. Adhes. Sci.* **2015**, *3*, 28. [[CrossRef](#)]
14. Currat, R.; Janssen, T. Excitations in Incommensurate Crystal Phases. *Solid State Phys. Adv. Res. Appl.* **1988**, *41*, 201–302. [[CrossRef](#)]
15. Dubois, J.-M. A model of wetting on quasicrystals in ambient air. *J. Non-Cryst. Solids* **2004**, *334–335*, 481–485. [[CrossRef](#)]
16. Souza, T.A.; Silva, D.D.S.; Júnior, F.W.E.L.A.; Feitosa, F.R.P.; Gomes, R.; Guedes, B. Analysis of the surface properties of Al-Cu-Fe-B and Al-Co-Cu quasicrystalline coatings produced by HVOF. *MRS Commun.* **2021**, *11*, 873–878. [[CrossRef](#)]
17. Mora, J.; García, P.; Muelas, R.; Agüero, A. Hard quasicrystalline coatings deposited by hvof thermal spray to reduce ice accretion in aero-structures components. *Coatings* **2020**, *10*, 290. [[CrossRef](#)]

18. Parsamehr, H.; Chen, T.-S.; Wang, D.-S.; Leu, M.-S.; Han, I.; Xi, Z.; Tsai, A.-P.; Shahani, A.-J.; Lai, C.-H. Thermal spray coating of Al-Cu-Fe quasicrystals: Dynamic observations and surface properties. *Materialia* **2019**, *8*, 100432. [[CrossRef](#)]
19. Minevski, Z.; Tennakoon, C.L.; Anderson, K.C.; Nelson, C.J.; Burns, F.C.; Sordelet, D.J.; Haering, C.W.; Pickard, D.W. Electrodeposited quasicrystalline coatings for non-stick wear resistant cookware. *Mater. Res. Soc. Symp. Proc.* **2003**, *805*, 345–350. [[CrossRef](#)]
20. Parsamehr, H.; Chang, S.Y.; Lai, C.H. Mechanical and surface properties of Aluminum-Copper-Iron quasicrystal thin films. *J. Alloys Compd.* **2018**, *732*, 952–957. [[CrossRef](#)]
21. Dos Barros, T.P.; de Cavalcante, D.G.; De Oliveira, D.F.; Caluête, R.E.; De Lima, S.J.G. Study of the surface properties of the epoxy/quasicrystal composite. *J. Mater. Res. Technol.* **2019**, *8*, 590–598. [[CrossRef](#)]
22. Anand, K.; Fournée, V.; Prévot, G.; Ledieu, J.; Gaudry, É. Nonwetting Behavior of Al-Co Quasicrystalline Approximants Owing to Their Unique Electronic Structures. *ACS Appl. Mater. Interfaces* **2020**, *12*, 15793–15801. [[CrossRef](#)]
23. Dubois, J.-M. *Useful Quasicrystals*; World Scientific: Singapore, 2005.
24. Weisbecker, P.; Bonhomme, G.; Bott, G.; Dubois, J.-M. The oxidation at 500 °C of AlCuFe quasicrystalline powders: A X-ray diffraction study. *J. Non-Cryst. Solids* **2005**, *351*, 1630–1638. [[CrossRef](#)]
25. Janot, C.; Dubois, J.-M. Les quasicristaux: Matières à paradoxes. In *3 La Métallurgie des Quasicristaux*; EDP SCIENCES: Paris, France, 1998; pp. 107–220. [[CrossRef](#)]
26. Wenzel, R.N. Resistance of solid surfaces to wetting by water. *Eng. Chem.* **2015**, *28*, 988–994. [[CrossRef](#)]
27. Good, R.J. Contact angle, wetting and adhesion. *J. Adhes. Sci. Technol.* **1992**, *6*, 1269–1302. [[CrossRef](#)]
28. Cassie, B.D. Wettability of porous surfaces. *Trans. Faraday Soc.* **1944**, *40*, 546–551. [[CrossRef](#)]
29. Pinhero, P.J.; Sordelet, D.J.; Anderegg, J.W.; Brunet, P.; Dubois, J.-M.; Thiel, P.A. Room temperature oxidation of Al-Cu-Fe and Al-Cu-Fe-Cr quasicrystals. *Mater. Res. Soc. Symp. Proc.* **1999**, *553*, 263–268. [[CrossRef](#)]
30. Brien, V.; Khare, V.; Herbst, F.; Weisbecker, P.; Ledeuil, J.B.; De Weerd, M.C.; Machizaud, F.; Dubois, J.-M. Influence of boron content on the microstructure of sintered Al_{62.5-x}Cu_{25.3}Fe_{12.2}B_x alloys (x = 0, 3, 5). *J. Mater. Res.* **2004**, *19*, 2974–2980. [[CrossRef](#)]
31. Belin-Ferré, E.; Dubois, J.-M.; Brunet, P. Potential Applications of Quasicrystalline Materials. In *Quasicrystals, Current Topics*; World Scientific: Singapore, 2000; pp. 498–532. [[CrossRef](#)]
32. Binnig, G.; Rohrer, H.; Gerber, C.; Weibel, E. Surface Studies by Scanning Tunneling Microscopy. *Phys. Rev. Lett.* **1982**, *49*, 57–61. [[CrossRef](#)]
33. Surface Tension Components and Molecular Weight of Selected Liquids. Available online: https://www.accudynetest.com/surface_tension_table.html (accessed on 1 April 2023).
34. Fowkes, F.M. Attractive Forces at Interfaces. *Ind. Eng. Chem.* **1964**, *56*, 40–52. [[CrossRef](#)]
35. Fox, H.W.; Zisman, W.A. The spreading of liquids on the low energy surfaces. I. Polytetrafluoroethylene. *J. Colloid Sci.* **1950**, *5*, 514–531. [[CrossRef](#)]
36. Bhushan, B. Surface roughness analysis and measurement techniques. In *Modern Tribology Handbook, Two Volume Set*; CRC Press: Boca Raton, FL, USA, 2000; pp. 49–119. [[CrossRef](#)]
37. De Oliveira, R.R.L.; Albuquerque, D.A.C.; Cruz, T.G.S.; Yamaji, F.M.; Leite, F.L. Measurement of the Nanoscale Roughness by Atomic Force Microscopy: Basic Principles and Applications. In *Atomic Force Microscopy-Imaging, Measuring and Manipulating Surfaces at the Atomic Scale*; BoD: London, UK, 2012. [[CrossRef](#)]
38. Demange, V.; Anderegg, J.W.; Ghanbaja, J.; Machizaud, F.; Sordelet, D.J.; Besser, M.; Thiel, A.P.; Dubois, J.-M. Surface oxidation of Al-Cr-Fe alloys characterized by X-ray photoelectron spectroscopy. *Appl. Surf. Sci.* **2001**, *173*, 327–338. [[CrossRef](#)]
39. Pinhero, P.J.; Anderegg, J.W.; Sordelet, D.J.; Besser, M.F.; Thiel, P.A. Surface oxidation of Al-Cu-Fe alloys: A comparison of quasicrystalline and crystalline phases. *Philos. Mag. B* **1999**, *79*, 91–110. [[CrossRef](#)]
40. Feitosa, F.R.P.; Gomes, R.M.; Silva, M.M.R.; Guedes de Lima, J.S.; Dubois, J.-M. Effect of oxygen/fuel ratio on the microstructure and properties of HVOF-sprayed Al₅₉Cu_{25.5}Fe_{12.5}B₃ quasicrystalline coatings. *Surf. Coat. Technol.* **2018**, *353*, 171–178. [[CrossRef](#)]
41. Bancel, P.A.; Heiney, P.A.; Stephens, P.W.; Goldman, A.I.; Horn, P.M. Structure of rapidly quenched Al-Mn. *Phys. Rev. Lett.* **1985**, *54*, 2422–2425. [[CrossRef](#)] [[PubMed](#)]
42. Vanderbilt, D.; King-Smith, R.D. Electric polarization as a bulk quantity and its relation to surface charge. *Phys. Rev. B* **1993**, *48*, 4442–4455. [[CrossRef](#)] [[PubMed](#)]
43. Barthes-Labrousse, M.G.; Dubois, J.-M. Quasicrystals and complex metallic alloys: Trends for potential applications. *Philos. Mag.* **2008**, *88*, 2217–2225. [[CrossRef](#)]

Disclaimer/Publisher’s Note: The statements, opinions and data contained in all publications are solely those of the individual author(s) and contributor(s) and not of MDPI and/or the editor(s). MDPI and/or the editor(s) disclaim responsibility for any injury to people or property resulting from any ideas, methods, instructions or products referred to in the content.